Yichen Qian, Mark R. Gilbert, Lucile Dezerald, Duc Nguyen-Manh, David Cereceda

Ab initio study of tungsten-based alloys under fusion power-plant conditions

Ab initio study of tungsten-based alloys under fusion power-plant conditions

Yichen Qian, Mark R. Gilbert, Lucile Dezerald, Duc Nguyen-Manh,
David Cereceda

Ab initio study of tungsten-based alloys under fusion power-plant conditions

Yichen Qian[1], Mark R. Gilbert[2], Lucile Dezerald[3], Duc Nguyen-Manh[2], David Cereceda[1]

[1] Department of Mechanical Engineering, Villanova University, Villanova, PA 19085, USA

[2] United Kingdom Atomic Energy Authority, Culham Centre For fusion Energy, Culham Science Centre, Abingdon, Oxon, OX14 3DB, UK

[3] Department of Materials Science and Engineering, Institut Jean Lamour, Universite de Lorraine, F-54011 Nancy, France

E-mail: `david.cereceda@villanova.edu`

Abstract. Tungsten (W) is considered a leading candidate for structural and functional materials in future fusion energy devices. The most attractive properties of tungsten for magnetic and inertial fusion energy reactors are its high melting point, high thermal conductivity, low sputtering yield, and low long-term disposal radioactive footprint. However, tungsten also presents a very low fracture toughness, primarily associated with inter-granular failure and bulk plasticity, limiting its applications. In recent years, several families of tungsten-based alloys have been explored to overcome the aforementioned limitations of pure tungsten. These might include tungsten-based high-entropy alloys (W-HEAs) and tungsten-based Self-passivating Metal Alloys with Reduced Thermo-oxidation or "SMART alloys" (W-SAs). Given their proximity to the plasma, it is crucial to understand how the exposure of these candidate plasma-facing materials (PFMs) to the neutron fluxes expected in fusion reactors impacts their material behavior over time. In this work, we present a computational approach that combines inventory codes and first-principles DFT electronic structure calculations to understand the behavior of transmuting tungsten-based PFMs. In particular, we calculate the changes in the chemical composition, production uncertainties, the elastic and ductility properties, and the density of states for five tungsten-based PFMs when exposed to EU-DEMO fusion first wall conditions for ten years.

1. Introduction

Tungsten (W) is considered as a leading candidate for plasma-facing applications in magnetic fusion energy devices. The most attractive properties of W for MFE are its high melting point and thermal conductivity, low sputtering yield and low long-term disposal radioactive footprint. These advantages are accompanied unfortunately by very low fracture toughness characterized by brittle trans- and inter-granular failure, which severely restricts its operating temperature window [1].

In recent years, several families of tungsten-based alloys have been explored to overcome the aforementioned limitations of pure tungsten. High-entropy alloys (HEAs) are a promising class of materials with remarkable properties [2–5]. They were originally conceived in the early 2000s as a blend of five or more elements with individual concentrations between 5 and 35 atom percent [6]. Interestingly, the composition stability of different HEAs phases is strongly correlated with the valence electron concentration from electronic structure analysis [7]. In particular, tungsten-based HEAs (W-HEAs) have shown superior mechanical properties at high temperatures, a superior melting point (above 2873 K), enhanced radiation resistance to heavy ion irradiation, and negligible radiation hardening when compared to pure tungsten [8–13]. Another attractive option are the so-called tungsten-based "SMART alloys" (W-SAs) that can adapt their behavior to the environment [14–18]. For example, in the event of a loss-of-coolant accident (LOCA) combined with an air ingress, W-SAs containing small amounts of Ti or Y have demonstrated the capability to create stable oxides that prevent their mobilization into the atmosphere.

Given their proximity to the plasma, the exposure of tungsten-based PFMs to neutron fluxes causes nuclear reactions that change the nuclide composition over time, a process known as transmutation. If this process leads to the production of radionuclides, then materials can become activated, while both direct reactions and reaction-decay chains can also produce nuclides of new elements. Both activation and transmutation are commonly observed in fields such as nuclear fission, nuclear fusion, astrophysics, nuclear security, and medical research. Since activation can create hazard and transmutation can change material performance, it is vital to carefully understand the nuclear reaction rates. Inventory codes are frequently used to predict the response of materials to a specific neutron irradiation field. Such an approach consists of numerically solving a set of coupled differential equations that describe the rate of change of all possible nuclides and thus evolve the nuclide composition in time [19, 20].

Experimentally, neutron irradiation campaigns at the fast test reactor Joyo [21–26], the Japan Materials Testing Reactor (JMTR) [25–27], and the High Flux Isotope Reactor (HFIR) [25, 26, 28–31] have investigated the microstructural evolution of tungsten and tungsten alloys. Their results indicate, for example, that the impact of Re and Os transmutation on the properties of materials after irradiation is at least as relevant as the displacement damage. Meanwhile, the current lack of experimental reactors and materials testing facilities that fully represent the conditions for making fusion a commercially feasible energy source

has motivated multi-scale materials modeling efforts to investigate the irradiation and temperature effects expected in fusion power plants [32–50]. These approaches, frequently based on first-principles calculations, have demonstrated their ability to provide quantitative and qualitative predictions of the material behavior in such extreme environments.

Despite the recent experimental advances in Joyo, JMTR, and HFIR, and the numerous efforts in the literature to investigate the effects of alloying elements on various properties of tungsten-based materials such as phase phase stability [51–55], elastic properties [51–54,56–58], ideal tensile strength [54,59], ductility [60], radiation defects [12,52,61], point defects [51,61–66], screw dislocation structure [67,68], grain boundaries [69], etc., to the best of our knowledge there is still a lack of understanding on how the thermomechanical behavior of tungsten-based PFMs change due to nuclear transmutation. In this work, we present a novel approach that integrates nuclear science and first-principles DFT electronic structure methods to better understand the neutron irradiation effects in PFMs.

Our paper is organized as follows. After this introduction, we provide in Section 2 an overview of the computational methods employed. The results are given in Section 3, which includes: (i) the changes in the chemical composition during the course of irradiation due to transmutation; (ii) the calculation of the equilibrium lattice constant, elastic properties, density of states, generalized stacking fault energy, unstable stacking fault energy, gamma surface, and dislocation-based ductility parameter of five tungsten-based candidate materials at the beginning of their operational life; and (iii) the effects of irradiation on these properties. We finalize in Section 4 with a brief discussion and the conclusions in Section 5.

2. Computational methods

The transmutation properties of tungsten-based PFMs in a fusion-like environment were characterized by using the FISPACT-II inventory code developed and maintained by the United Kingdom Atomic Energy Authority over the last 30 years. FISPACT-II [19, 20] solves coupled differential equations describing the rate of change of all possible nuclides and thus evolves a nuclide composition in time. For the present work, a $\underline{\phi}(E)$ vector of neutron fluxes (as a function of energy E) was taken from neutron transport calculations performed for a recent conceptual design (see [70,71] for details) for EU-DEMO; a demonstration fusion power plant being researched in Europe [72,73]. Specifically, the energy-flux spectrum for the outer equatorial first wall of the torus-shaped tokamak has been used, which is predicted to be one of the highest flux regions of a fusion reactor (second only to the inner equator). The total flux ϕ for this spectrum was 2.1×10^{14} n cm^{-2} s^{-1}. FISPACT-II calculations evolved the initial composition of the five tungsten-based materials shown in Table 1 in this neutron environment for 10 continuous full-power years.

Note for the present calculations, in contrast to those reported previously in [74], here self-shielding has been properly accounted for in the inventory simulations with FISPACT-II. This results in slightly reduced transmutation rates of certain elements, particularly W and Ta, which would otherwise have high burn-up rates due to over-predicted impact

of giant neutron capture resonances, consequently leading to over-predicted production of transmutants such as Re – see [19, 75, 76] for more details on the self-shielding phenomenon and the importance of including appropriate corrections in transmutation predictions of W and its periodic-table neighbors.

Table 1: Chemical composition of the five tungsten-based materials considered in this study at the beginning of their operational life.

	Chemical composition (at%)					
	W	Cr	Ti	Y	Ta	V
Tungsten (W)	100	-	-	-	-	-
W smart alloy (SA1) [16]	67.16	26.98	5.86	-	-	-
W smart alloy (SA2) [17]	67.93	31.11	-	0.958	-	-
W high-entropy alloy (HEA1) [77]	25	25	25	-	25	-
W high-entropy alloy (HEA2) [77]	25	-	25	-	25	25

For their part, Density Functional Theory (DFT) calculations were performed by using the open-source software distribution QUANTUM ESPRESSO [78, 79]. Following our recent work on first-principles calculations of transmuting tungsten [74], we employed the local-density approximation (LDA) with the Perdew-Burke-Ernzerhof (PBE) parametrization [80] in the formulation of the exchange correlation functional. Furthermore, the virtual crystal approximation (VCA) [81] was used to simulate the variety of tungsten-based alloys that result from transmutation. Optimized Norm-Conserving Vanderbilt Pseudopotentials [82] compatibles with the VCA were used in our non-spin polarized calculations.

The elastic properties were calculated using a conventional 2-atom bcc supercell, a shifted $22 \times 22 \times 22$ grid Monkhorst–Pack k-mesh [83], and a planewave cutoff energy of 110 Ry (~ 1496.63 eV). For their part, the calculation of the gamma surfaces, generalized stacking fault energies (GSFE), and the dislocation-based ductility parameter were performed in a 14-atom bcc supercell, with an energy cutoff of 90 Ry (~ 1224.51 eV), and Brillouin zones sampled by a shifted $24 \times 24 \times 1$ grid. The convergence tests to choose these energy cutoff and k-points values are provided in Appendix ?. The reader is referred to our previous work [74] for more details on how we extract elastic and plastic properties from the energies calculated via DFT simulations.

3. Results

3.1. Nuclear transmutation

Figure 1 shows how the composition of the five tungsten-based PFMs shown in Table 1 changed during the course of irradiation due to transmutation. The graph shows the concentrations, both in atomic percent (at.%) and in atomic parts per million (appm), on

a logarithmic scale of the elements created during the course of the irradiation. Even after 10 years of irradiation, and despite W and Ta, in particular, being susceptible to high transmutation rates, all the tungsten-based PFMs studied would still be predominantly composed of the elments in their initial chemical making-up.

To gain a deeper understanding of how the chemical composition changes during the course of irradiation we also plotted the concentration gradient $\Delta c = c(t) - c(0)$ in Figure 2 for the top seven elements in each material, where $c(t)$ is the chemical composition after t years of irradiation and $c(0)$ is the initial composition of the material. The elements included in the second plots of the transmutation results are the ones that will be considered in the formulation of the DFT pseudopotential below. The final compositions at 10 years of these alloys are listed in table A1. These results show how the profile of burn-up or growth of each element in the composition (both those originally present and those created by transmutation) varies for the different initial alloy compositions. For example, the rate of production of tungsten decreases in pure W and W-SAs while it increases in the W-HEAs (due to its production from the burn-up of Ta in those alloys). The concentration of Re, a primary transmutant, increases in all five materials (produced from W), while the concentration of Ta decreases (is burnt-up) in both W-HEAs (it is one of the initial alloysing elements) and increases in pure W and the W-SAs.

As previously [74], we can obtain the time-averaged % errors in the transmutation predictions due to the evaluated uncertainties in the nuclear reaction data (from TENDL-2017 [84]). As standard, FISPACT-II computes errors in the concentrations of the dominant radionuclides in a material after irradiation, by summing in quadrature the uncertainty on each reaction in each production chain (or pathway) of the radionuclide. Typically there maybe several pathways of production for each nuclide; for example, after 10 years of irradiation, four reaction chains are found to be important for the production of ^{186}Re (half-life, $T_{1/2} = 3.7$ days) in pure W, involving various combinations of neutron capture (n,γ) and neutron multiplication (n,2n) reactions, as well as β^- decay – FISPACT-II correctly combines the uncertainties across all reactions and chains to calculate the overall uncertainty in ^{186}Re.

For the present work, we have employed a modified version of FISPACT-II, where uncertainties are also evaluated for the production of stable nuclides of the main transmutant elements. The methodology is the same, whereby FISPACT-II uses a tree-search algorithm [19] to identify the contributing pathways for a given nuclide before propagating uncertainties along each chain, but here we enforce a requirement for even stable nuclides to receive this evaluation. To compute the final, total uncertainty of production for a complete element, we sum in quadrature the absolute uncertainties in concentration from the individual nuclides.

Table 2 shows the time-averaged (i.e. the average uncertainty in each element across the 10 different irradiation times) % uncertainties for each significant element (either original or transmutant) in the material. Note that the uncertainty quantification (UQ) approach

177 used here, only calculates the *production* uncertainty on each nuclide (hence each element)
178 – i.e. contributions to a nuclide's uncertainty only come from propagating uncertainties
179 along reaction chains where that nuclide is an end point or daughter. Uncertainties in the
180 burn-up or *depletion* of nuclides, which are particularly relevant for nuclides that formed
181 the initial composition of a material, are not included here (other than indirectly in the way
182 those depletion uncertainties, represented by the initial reactions in each production chain,
183 contribute to production uncertainties elsewhere). Future work will consider a methodology
184 to combine production and depletion uncertainties.

Table 2: Time-averaged % errors in elemental concentrations predicted by FISPACT-II for each component (original present elements and new transmutant products) in the alloys during the course of the 10-year power-plant first wall irradiation. Error estimates for transmutants are only given if their concentrations reach 1 appm during the 10 years (see main text for details).

Material elements	W	SA1	SA2	HEA1	HEA2
W	0.12[‡]	0.12[‡]	0.12[‡]	0.64[‡]	0.65[‡]
Re	9.15[‡]	9.07[‡]	9.08[‡]	8.64[‡]	8.57[‡]
Ta	36.20[‡]	36.22[‡]	36.22[‡]	0.22[‡]	0.22[‡]
Os	7.76[‡]	9.94[‡]	9.95[‡]	9.58	10.55[‡]
Hf	31.36[‡]	31.38	31.38	30.81[‡]	30.82[‡]
He	43.16[‡]	45.64	53.85	34.10	27.86
H	73.56[‡]	41.41	44.33	38.29	41.84
Cr	–	0.002[‡]	0.002[‡]	0.002[‡]	4.55
Ti	–	0.13[‡]	44.15	0.04[‡]	0.04[‡]
V	–	28.89[‡]	28.93[‡]	28.87[‡]	0.05[‡]
Sc	–	18.04	–	18.04	18.03
Ca	–	70.55	–	70.66	70.65
Mn	–	10.59	10.59	10.58	–
Y	–	–	0.01[‡]	–	–
Sr	–	–	35.62	–	–
Zr	–	–	6.72	–	–

[‡] transmutation elements considered in pseudopotential generations of W-based alloys

185 Notwithstanding the above caveat, it is clear from Table 2 that uncertainties are small for
186 for elements that were present in the initial compositions of the five materials, demonstrating
187 that the growth rates for those elements, coming from the sum across all nuclides (stables
188 and created unstables), are relatively small compared to the reservoir of original atoms of
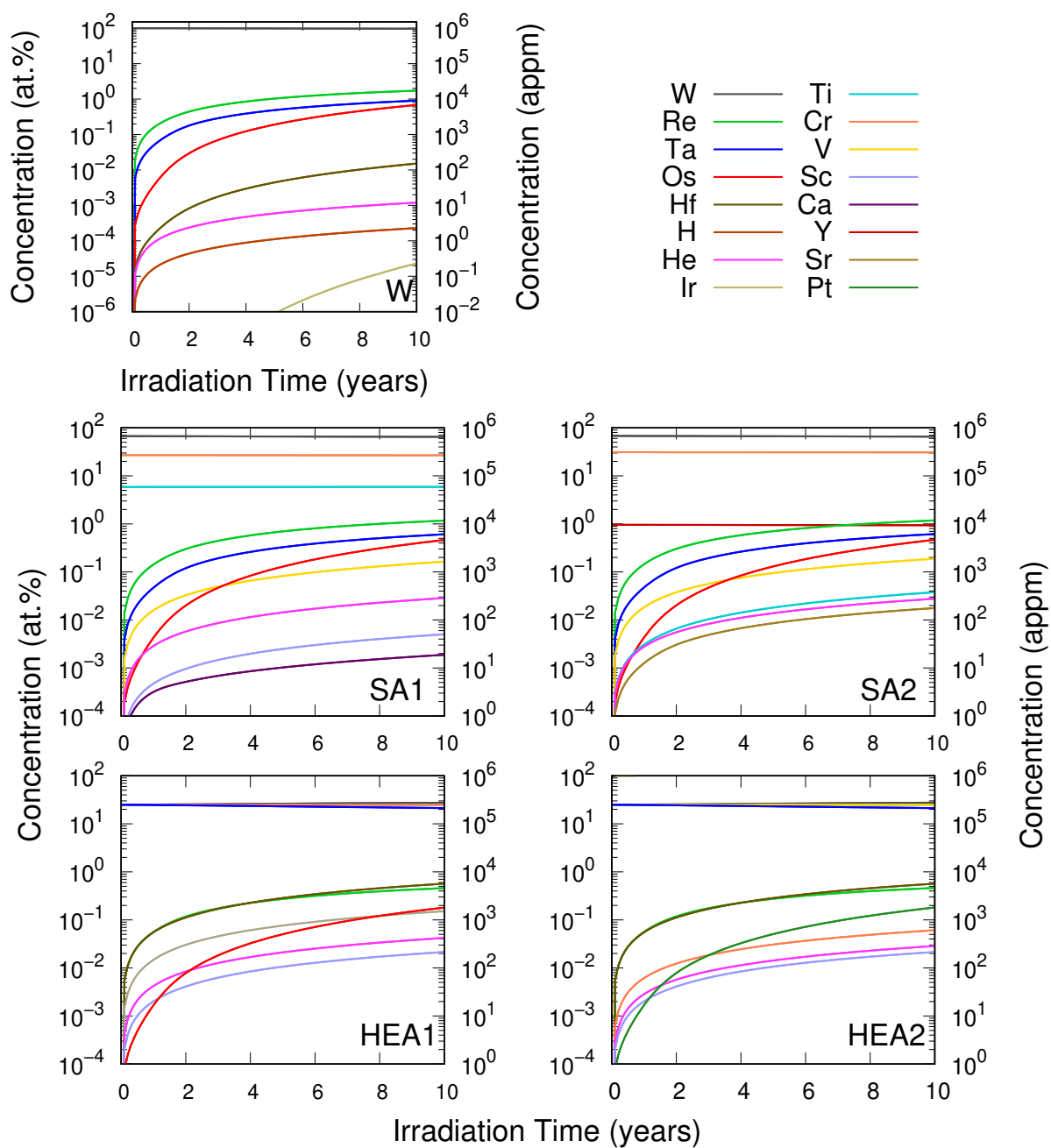189 those elements.

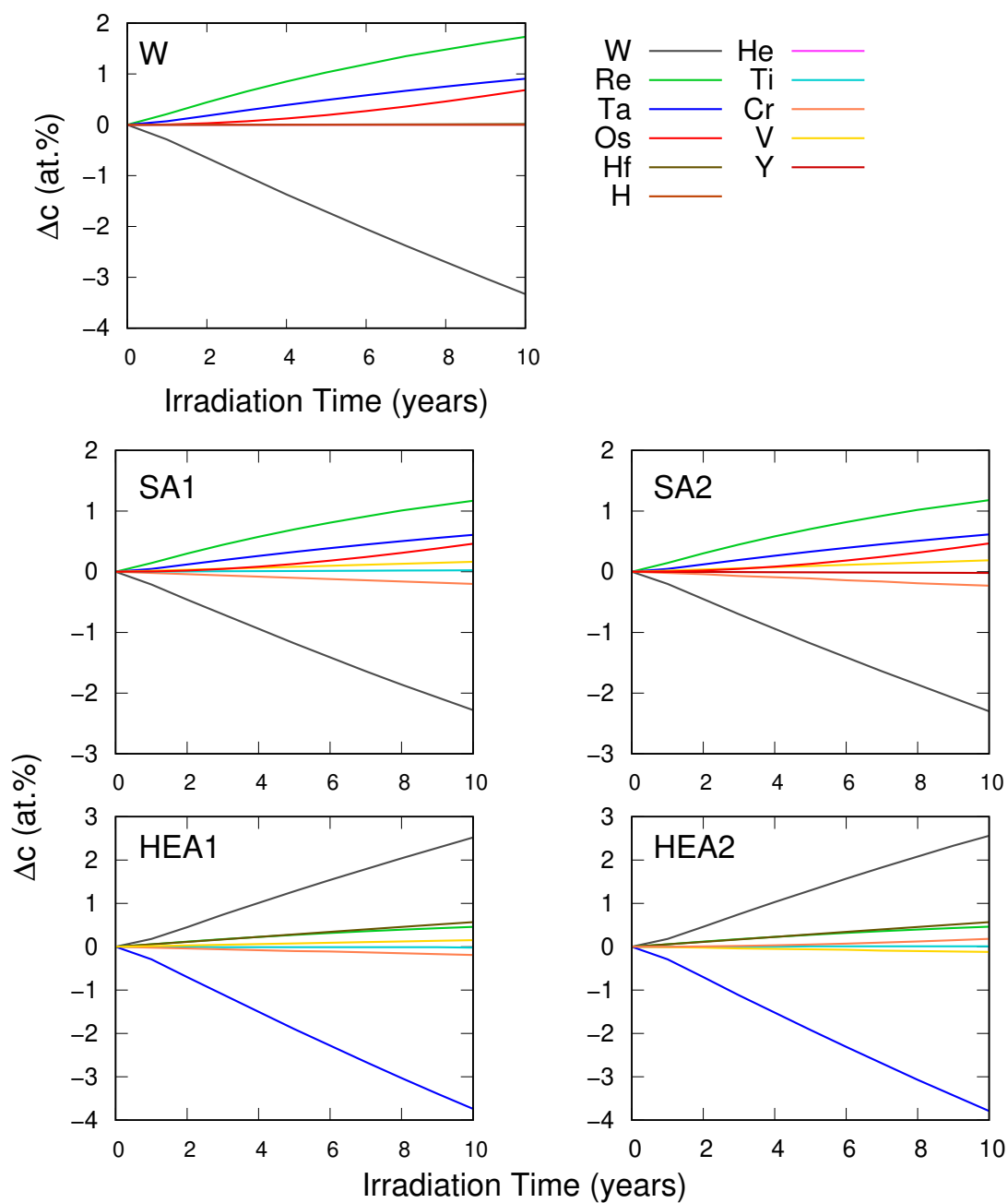Figure 1: Transmutation of W-based alloys during a 10-year irradiation.

Figure 2: Concentration gradient of W-based alloys during a 10-year irradiation period. $\Delta c = c(t) - c(0)$, where $c(t)$ is the chemical composition after t years of irradiation and $c(0)$ is the initial composition of the material.

On the other hand, for transmutant elements newly created by the irradiation exposure (compare table 1 to table A1), where the production uncertainty is dominant, the results show that uncertainties in predictions can be reasonably high – as much as 70% in some cases. Such uncertainties are not uncommon in inventory predictions, particularly for minor (rare) components of a nuclide inventory, but it is vital that they are are provided as part of any transmutation or activation analysis, both to appreciate the significance (or not) of the quantity to which they correspond, but also so that they could be used to define engineering safety factors in the design of fusion reactors. It has been observed, for example, that there is a potential 20-25% over-prediction compared to experimental measurements of the decay heat (measured in kW) in W after exposure to a fusion environment – in that case a low flux deuterium-tritium fusion neutron source (FNS) – where the primary reaction pathway responsible, $^{186}W(n,2n)^{185}W$, has a $\sim$7% uncertainty in the FNS spectrum with TENDL-2017 (see [85], based on data from [86]); whilst an over-prediction is not ideal because of the potential cost of unnecessary cooling engineering, such a prediction, with the data uncertainties, can be used to ensure sufficient cooling and thus safe reactor operation.

3.2. Material behavior at $t = 0$

In Table 3, we list the equilibrium lattice constant, single-crystal elastic constants, and polycrystalline elastic properties for five tungsten-based PFMs at the beginning of their operational life, i.e. at time $t = 0$, with the chemical compositions shown in Table 1. While we could not find other works in the literature providing such a comprehensive study for the tungsten-based alloys, Tables 2 and 3 in [74] show that the results obtained for pure W are consistent with their counterparts from previous experimental and theoretical works. These results also indicate the crucial role chemical composition plays in the elastic response of the material. For example, the elastic properties obtained for SA1 and SA2, whose chemical compositions still have W as the primary element (> 67 at%), are closer to those from pure W, especially when compared with the four-components HEA1 and HEA2 equiatomic alloys.

Figure 3 shows the generalized stacking fault energy (GSFE) curves on both $\langle 1\,1\,1\rangle\{\bar{1}\,1\,0\}$ and$\langle 1\,1\,1\rangle\{1\,1\,\bar{2}\}$ slip systems for the five tungsten-based PFMs at the beginning of their operational life, i.e., with the chemical compositions shown in Table 1. The figures reveal several interesting trends that are consistent with previous works in the field. Firstly, the unstable stacking fault energy γ_{us}, defined as the maximum value of the GSFE curve, is always in the middle of the energy path from one equilibrium position to another on a $\{\bar{1}\,1\,0\}$ plane while there is certain asymmetry towards the first equilibrium position on a $\{1\,1\,\bar{2}\}$ plane [60, 87–91]. Secondly, γ_{us} is higher for the $\langle 1\,1\,1\rangle\{1\,1\,\bar{2}\}$ slip system [52, 60, 90–92]. Thirdly, taking pure W as a reference, we notice that the GSFE curve is lower for HEA1 and HEA2, and higher for SA1 and SA2. The specific values of γ_{us} are shown in Table 4, which also includes the surface energy γ_s and the dislocation-based ductility parameter $D = \gamma_s/\gamma_{us}$ formulated by Rice [93]. The effects of the chemical composition on the calculated γ_s are similar to those observed for γ_{us}, i.e., if we take pure W as the reference system, HEA1 and

Table 3: Theoretical equilibrium lattice parameter, single-crystal elastic constants, and polycrystalline elastic properties for the five tungsten-based PFMs at the beginning of their operational life, i.e., with the chemical compositions shown in Table 1: equilibrium lattice parameters a_0, bulk modulus B, elastic constants C_{ij}, tetragonal shear modulus C', shear modulus G and Young's modulus E.

	a_0 (Å)	C_{11} (GPa)	C_{12} (GPa)	C_{44} (GPa)	B (GPa)	C' (GPa)	G (GPa)	E (GPa)
W	3.1835	512.501	197.906	142.461	302.771	157.298	148.22	382.669
SA1	3.100	554.167	212.469	166.285	326.369	170.849	151.011	392.496
SA2	3.093	571.430	218.195	181.037	335.940	176.618	161.594	417.793
HEA1	3.144	351.731	195.262	107.702	247.419	78.235	86.934	233.460
HEA2	3.199	285.202	178.625	99.756	214.151	53.289	72.234	194.802

HEA2 have an inferior γ_s while SA1 and SA2 present a superior value. This implies, as it is shown in Table 4, that the dislocation-based ductility parameter D is higher in W-HEAs and lower in W-SAs.
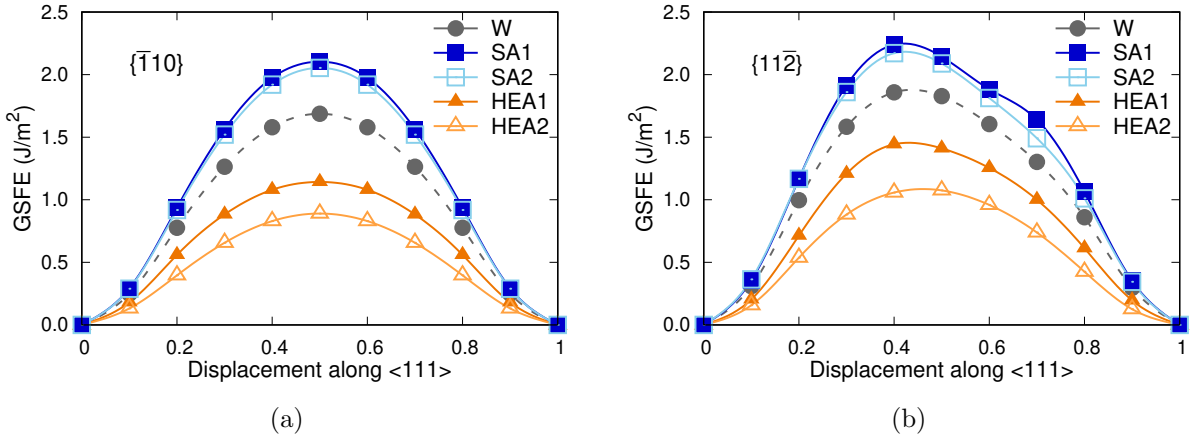

Figure 3: The general stacking fault energy for the initial composition of the five candidate PFMs along (a) $\{1\,1\,1\}\{\bar{1}\,1\,0\}$ and (b) $\{1\,1\,1\}\{1\,1\,\bar{2}\}$.

The impact of the alloying elements on the electronic structure of the five tungsten-based PFMs at the beginning of their operational life can be investigated via the density of states (DOS), which is shown in Figure 4. One can recognize, for W and the other alloys, the shape of the d band with a marked pseudo-gap, as expected for BCC transition metals. To compare the different alloys, the Fermi energy of each material E_F^{alloy} is taken as the reference energy. E_F^{alloy} values are listed in Table 5, together with the number of valence electrons for each of the candidate PFMs. These results reveal the different nature of the two families of tungsten-based alloys studied here: W-SAs show slight variations of the valence charge and

Table 4: Theoretical surface energy γ_s, unstable stacking fault energy γ_{us}, and dislocation-based ductility parameter D for the five tungsten-based PFMs at the beginning of their operational life, i.e., with the chemical compositions shown in Table 1. The calculations have been performed in both $\{1\,1\,1\}\{\bar{1}\,1\,0\}$ and $\{1\,1\,1\}\{1\,1\,\bar{2}\}$ slip systems.

	$\langle 1\,1\,1 \rangle \{\bar{1}\,1\,0\}$			$\langle 1\,1\,1 \rangle \{1\,1\,\bar{2}\}$		
	γ_s (J/m^2)	γ_{us}(J/m^2)	D	γ_s(J/m^2)	γ_{us}(J/m^2)	D
W	3.308	1.687	1.961	3.762	1.875	2.006
SA1	3.869	2.103	1.839	4.474	2.243	1.994
SA2	3.874	2.054	1.887	4.447	2.178	2.042
HEA1	2.959	1.143	2.590	3.583	1.489	2.406
HEA2	2.888	0.890	3.246	3.450	1.085	3.179

the Fermi level compared to pure W, with a fermi level located in the pseudogap, while the decrease of valence charge for W-HEAs is more significant, lowering the Fermi energy. This results in a shift of the fermi level of HEAs to the left, outside the pseudo gap, as evidenced in Fig.4.

Table 5: Fermi energy E_F^{alloy}, number of valence electrons, and DOS values at Fermi energies for each of the five tungsten-based PFMs $t = 0$, i.e., with the chemical compositions shown in Table 1.

	E_F^{alloy} (eV)	No. valence e$^-$	DOS
W	21.942	14	0.855
SA1	21.771	13.883	0.545
SA2	22.287	13.971	0.590
HEA1	18.902	13.250	2.055
HEA2	17.858	13	2.604

The reader is referred to Appendix A for more details about the material behavior of the principal alloying elements of the tungsten-based PFMs shown in Table 1: Cr, Ta, Ti, and V. These include their equilibrium lattice parameter, single-crystal elastic constants, surface energy, unstable stacking fault energy, dislocation-based ductility parameter, Fermi energy, and DOS, among others.

3.3. Effects of irradiation on the behavior of tungsten-based PFMs

Given the extreme environments PFMs are exposed to, it is critical to understand both their behavior at $t = 0$ (cf. Section 3.2) and how their response evolves due to the changes in the chemical composition that occur through nuclear transmutation (cf. Section 3.1).
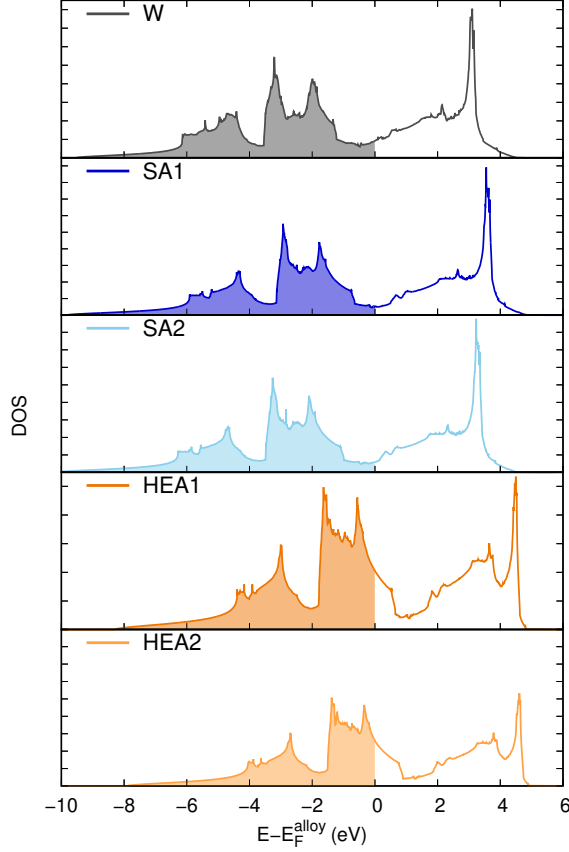
Figure 4: Total DOS of the candidate W-based materials at the beginning of their operational life. E_F^{alloy} is the Fermi energy of each material, and it is taken as the reference energy.

Our results of the irradiation effects on the five tungsten-based PFMs at 10 years is listed in Table 6 with the equilibrium lattice constant, single-crystal elastic constants, and polycrystalline elastic properties.

We noticed that the changes in these properties over time are less pronounced than the existing differences between the families of tungsten-based alloys before any irradiation occurs. As such, we decided not to plot the absolute trends. Instead, we choose to provide the initial and final values in Table 3 and Table 6, and represent the time evolution of the aforementioned properties in terms of the relative difference δ_X, defined as:

$$\delta_X = \frac{X_t - X_0}{X_0} \tag{1}$$

where X_0 is the value of the property of interest X at the beginning of the operational life of the material (t = 0 years) and X_t is the value of that same property after t years of exposure to the fusion conditions described in Section 2.

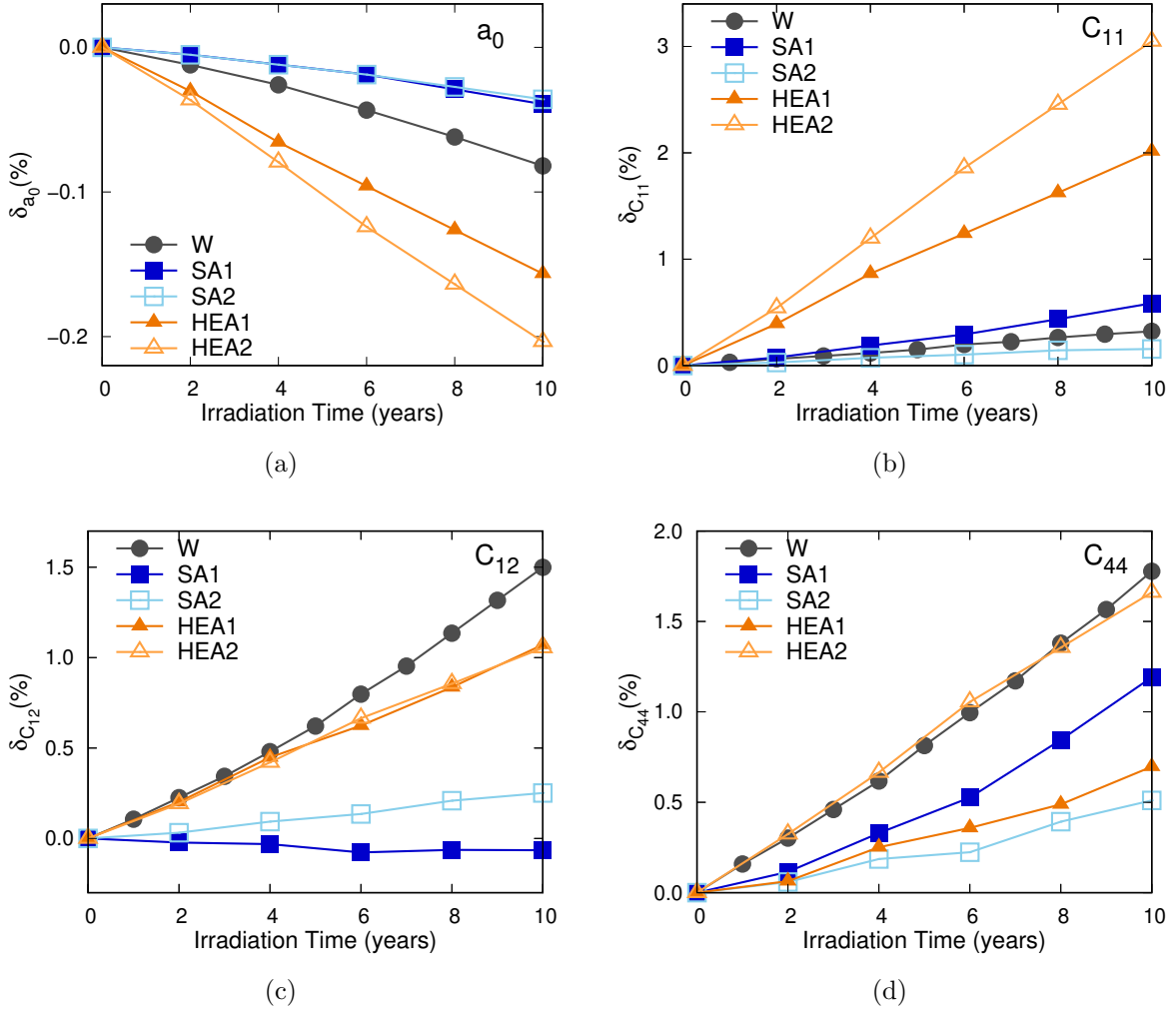Following this notation, Figure 5 and Figure 6 show the time dependence of the

Figure 5: Evolution of (a) the lattice constant a_0 and the elastic properties (b) C_{11}, (c) C_{12}, (d) C_{44} during the first ten years of irradiation under EU-DEMO first wall conditions.

equilibrium lattice constant, single-crystal elastic constants, and polycrystalline elastic properties as the chemical composition of the tungsten-based materials change due to irradiation. The observed linear behavior has been confirmed in previous experimental [94] and computational [54,67] measurements of W-Re alloys, as well as in our recent calculations on transmuting tungsten [74]. In advance of discussing these results and their implications in detail in the following section, we note the following features from the figures: (i) the relative difference δ after ten years of exposure is less than 7% for all the properties investigated. (ii) the lattice constant is the only measurement decreasing for all five tungsten-based PFMs as irradiation time (and therefore the relative concentration of transmutants) increases. C_{12} and C' show some materials with a flat or slightly negative slope. All other properties monotonically increase with irradiation time for all five tungsten-based PFMs; (iii) the
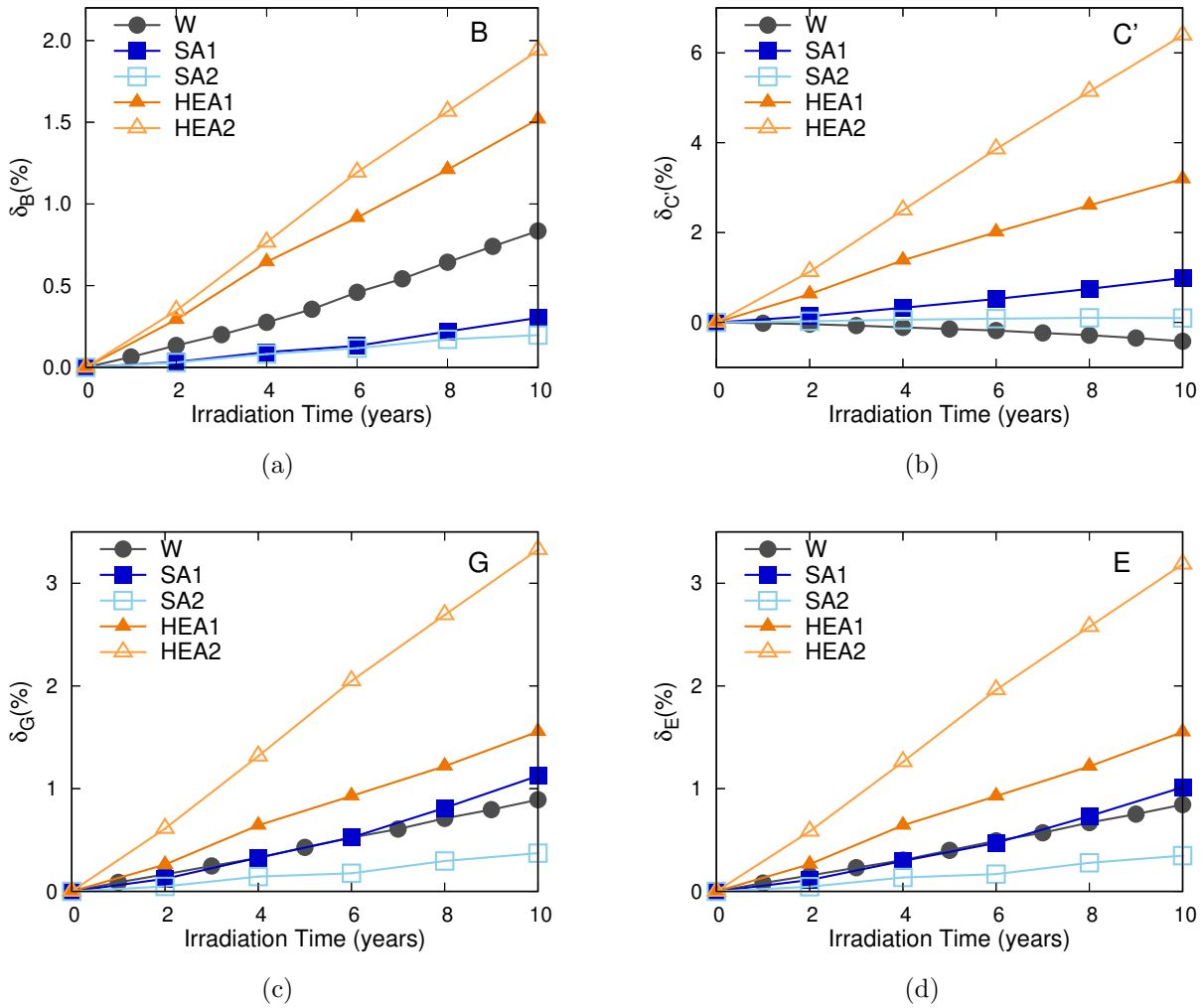
Figure 6: Evolution of (a) the bulk modulus B, (b) the tetragonal shear elastic constant C', (c) the shear modulus G, and (d) the Young's modulus E during the first ten years of irradiation under EU-DEMO first wall conditions.

magnitude of the slope is steeper for W-HEAs than for W-SAs. In particular, HEA2 presents the most prominent changes with irradiation for the majority properties and SA2 the smallest.

To illustrate the effects of nuclear transmutation on the electronic structure of the candidate PFMs, we plot in Figure 7 the total DOS of pure tungsten and transmuting tungsten after ten years of continuous exposure to EU-DEMO first wall conditions. These results indicate that the Fermi energy slightly increases after ten years, but the shape of the d band remains basically unchanged after irradiation. The relative difference δ of the integrated DOS for the five tungsten-based PFMs after 10 years or irradiation is also shown in Figure 8. The magnitude of maximum peak is always less than 1.5%, indicating that the differences between the integrated DOS over the entire energy range are very small.

Table 6: Theoretical equilibrium lattice parameter, single-crystal elastic constants, and polycrystalline elastic properties for the five tungsten-based PFMs at $t = 10$: equilibrium lattice parameters a_0, bulk modulus B, elastic constants C_{ij}, tetragonal shear modulus C', shear modulus (G) and Young's modulus (E).

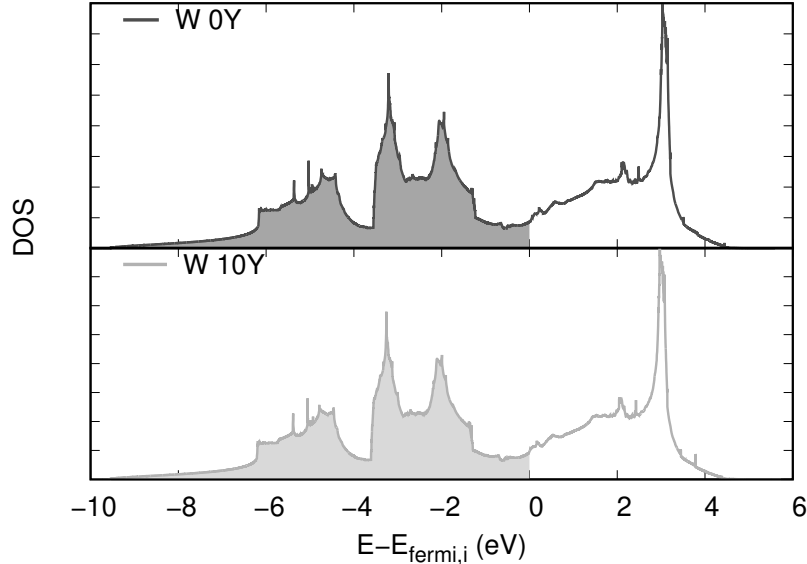|	a_0 (Å)	C_{11} (GPa)	C_{12} (GPa)	C_{44} (GPa)	B (GPa)	C' (GPa)	G (GPa)	E (GPa)
W	3.181	514.148	200.873	144.994	305.298	156.638	149.544	385.900
SA1	3.098	557.410	212.331	168.265	327.357	172.540	152.708	396.475
SA2	3.092	572.320	218.743	181.961	336.602	176.789	162.195	419.246
HEA1	3.139	358.815	197.354	108.453	251.174	80.731	88.286	237.082
HEA2	3.192	293.897	180.507	101.412	218.304	56.695	74.639	201.007

Figure 7: Comparison of the total DOS for pure W and transmuting W after 10 years or irradiation. E_{ref} is the Fermi energy of pure tungsten. Top: total DOS of pure W; Bottom: total DOS of transmuting W after 10 years of irradiation.

Despite these slight variations, we can still appreciate how the regions with a positive slope indicate an energy range where the integrated DOS of transmuting PFMs is higher than its counterpart at $t = 0$, and vice versa.

Next we calculate the evolution of the number of valence electrons during the first ten years of irradiation. The results are shown in Figure 9 for all five tungsten-based PFMs. Given that the observed changes in the absolute number of valence electrons are
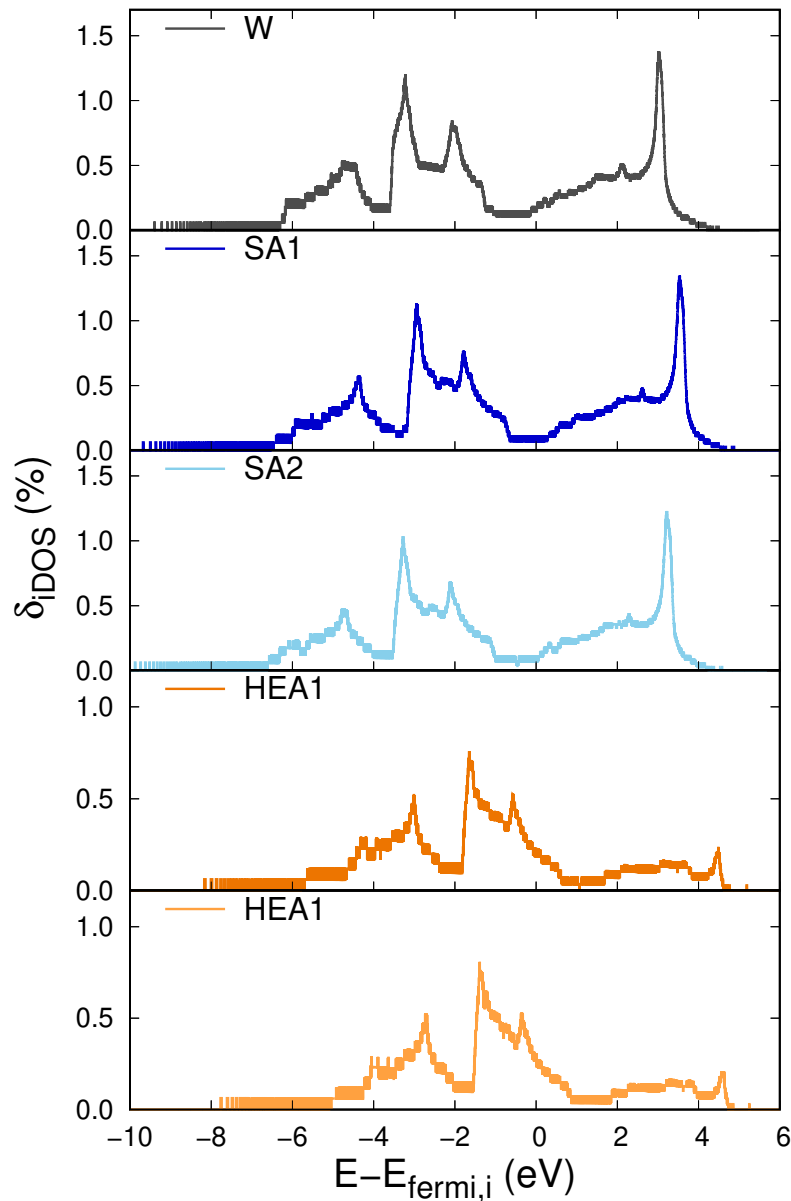
Figure 8: Relative difference δ of the integrated DOS for the five tungsten-based PFMs after 10 years or irradiation.

less pronounced than the existing differences between the families of tungsten-based alloys before any irradiation occurs, we decided to provide the initial values in Table 5 and represent the time evolution of the valence electrons in terms of the relative difference δ used before for the elastic properties (cf Eq. 1). Based on these results, all materials increased their number of valence electrons over time, and W-HEAs show a steeper slope than W-SAs. Still, these behaviors should be taken with caution, as the relative differences are always less than 0.3%.

In Figure 10 we provide the evolution of γ_{us} and γ_s for both $\langle 1\,1\,1 \rangle \{\bar{1}\,1\,0\}$ and
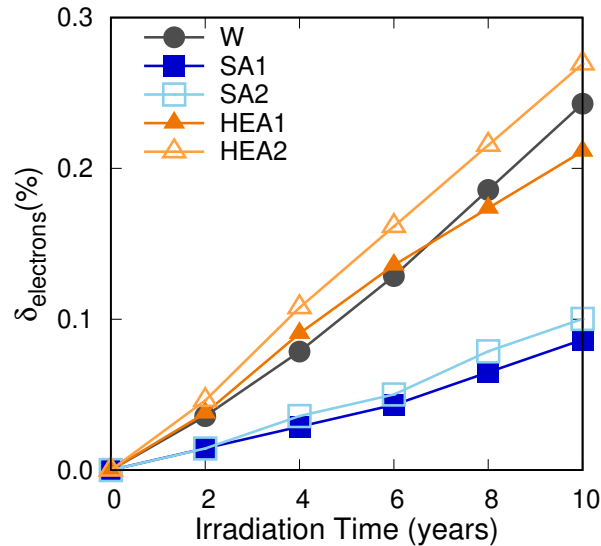
Figure 9: % change in the number of valence electrons for the five tungsten-based PFMs during the ten years of irradiation under EU-DEMO first wall conditions.

$\langle 1\,1\,1\rangle\{1\,1\,\bar{2}\}$ slip systems during the first ten years of irradiation under EU-DEMO first wall conditions. We choose to represent the irradiation effects on these properties in terms of the relative % difference δ for the same reasons discussed above when presenting the evolution of the elastic properties and the number of valence electrons. Several trends can be identified from these figures. Firstly, the changes on the γ_{us} are twice as pronounced as the changes on γ_s. That applies to all the materials and both slip systems. Secondly, the δ values of both properties are higher on the $\{1\,1\,\bar{2}\}\langle 1\,1\,1\rangle$ slip system for all the materials. Thirdly, a different evolution is observed depending on the chemical composition of the tungsten-based alloys. Both γ_{us} and γ_s monotonically increase on both slip systems for W-HEAs while they decrease or remain flat (depending on the property) for W-SAs. Furthermore, the magnitude of the slope is always steeper for W-HEAs than for W-SAs. For its part, W presents a more similar behavior to W-SAs, decreasing its γ_{us} and slightly decreasing its γ_s due to transmutation.

Once the irradiation effects on both γ_s and γ_{us} are calculated, the relative difference of the dislocation-based ductility parameter $D = \gamma_s/\gamma_{us}$ [93] is obtained. We present results for the two slip systems of interest in Figure 11. All the materials exhibit a linear behavior with irradiation time: W is the material with the steepest increase of ductility, followed by SA2; the variations on SA1 are negligible, while both W-HEAs show a decrease of ductility, being HEA2 the material experiencing the most significant drop. It is also worth noting that the increase on ductility for W and the W-SAs is more pronounced on the $\{\bar{1}\,1\,0\}\langle 1\,1\,1\rangle$ slip system.
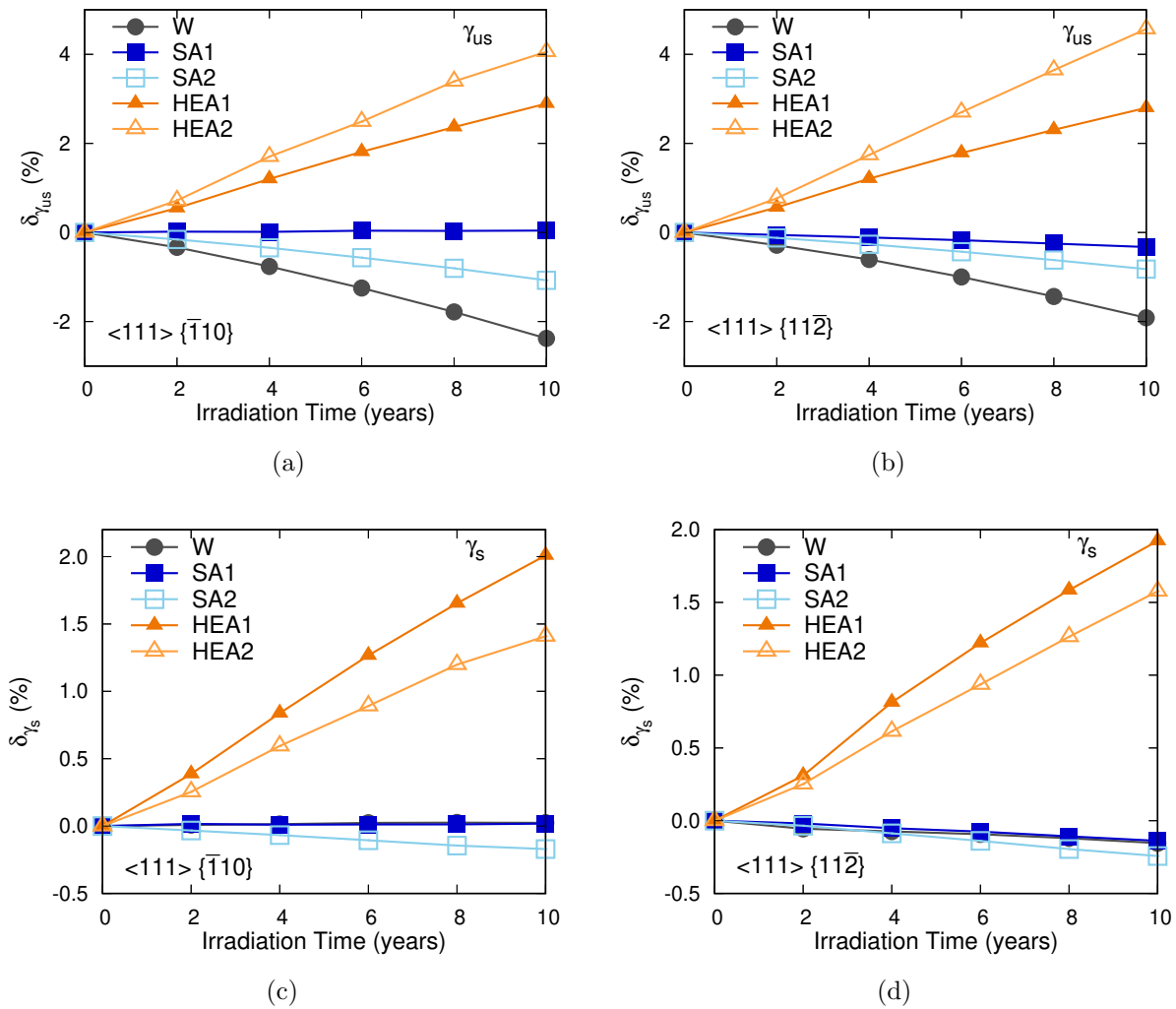
Figure 10: Evolution of (a) the unstable stacking fault energy γ_{us} for both $\{\bar{1}\,1\,0\}\langle 1\,1\,1\rangle$ slip system, (b) γ_{us} for $\{1\,1\,\bar{2}\}\langle 1\,1\,1\rangle$ slip system, the surface energy γ_s for $\{\bar{1}\,1\,0\}\langle 1\,1\,1\rangle$ slip system, and (d) γ_s $\{1\,1\,\bar{2}\}\langle 1\,1\,1\rangle$ during the first ten years of irradiation under EU-DEMO first wall conditions.
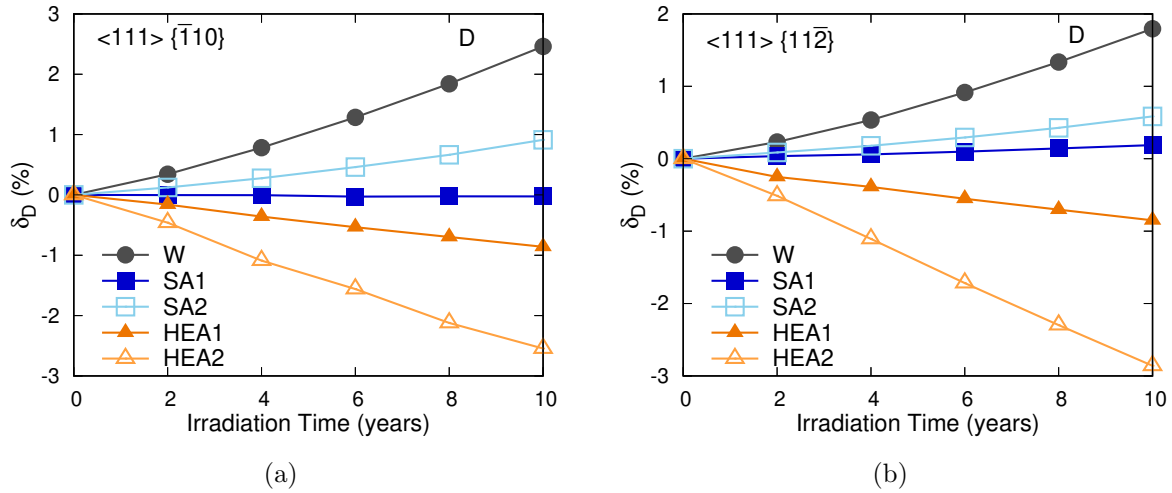
Figure 11: Evolution of the dislocation-based ductility parameter D for the five W-based materials along the (a) $\langle 1\,1\,1\rangle\{\bar{1}\,1\,0\}$ and (b) $\langle 1\,1\,1\rangle\{1\,1\,\bar{2}\}$ slip systems during the first ten years of continuous exposure to EU-DEMO first wall conditions.

4. Discussion

4.1. Material behavior at the beginning of the operational life

Section 3.2 presented the behavior of the tungsten-based PFMs before exposing them to a plasma-exposed environment expected in EU-DEMO. The results included calculations of the lattice parameter, elastic properties, general stacking fault energies, unstable stacking fault energies, gamma surfaces, dislocation-based ductility parameter, total DOS, Fermi energy, and number of valence electrons.

First, the comparison of the overall behavior of the two families of tungsten-based PFMs reveal that W-SAs present more similarities to pure W than W-HEAs. These observations, shown for example when comparing the total DOS in Fig. 4, are consistent with the chemical composition of the candidate materials and the fundamental nature of the VCA approach: the W-HEAs studied here are four-element equiatomic HEAs and the W-SAs contain a higher relative concentration of W.

Next, if we take pure W as the reference material, understanding why specific properties increase for W-HEAs and decrease for W-SAs, and vice versa, requires a more profound discussion supported by the study of the underlying effects of the individual alloying elements and their relative composition. For this purpose, we investigated in Appendix A the material behavior of the principal alloying elements, i.e.: Cr, Ta, Ti, and V. The results shown in Table 3, Table 4 and Fig. 3 reveal that the lattice constant is higher in W-HEAs, while all the other elastic properties and GSFE are higher in W-SAs. One contributing factor to these differences could be the presence of Ti in the W-HEAs: Ti, in a bcc phase, has negative elastic constants since the stable phase at low temperature is hcp (as evidenced in Appendix A).

Furthermore, the comparison between the two W-HEAs indicates that HEA2 is softer than HEA1. We find this consistent with the presence of V in HEA2 and Cr in HEA1 (cf. Table 1), the softer behavior of V with respect to Cr (cf. Table A2), and the expected hardening effect when reducing the lattice constant (cf. Table A2), and the relative changes in hardening when comparing different columns in the periodic table (V is Group V while Cr is group VI).

In terms of GSFE, γ_{us}, and the dislocation-based ductility parameter D, the presence of the different alloying elements (cf. Table 1) and their individual properties (as shown in Appendix A) play also a critical role explaining the behavior of the different tungsten-based candidate materials. For example, the presence of Ta in HEAs and its lower γ_{us} with respect to pure W (cf. Table A3) reduces γ_{us} of HEAs when compared to pure W and SAs. Similarly to the behavior observed with the elastic properties, the presence of V in HEA2 reduces its γ_{us} when compared to HEA1, which contains Cr.

The total electronic density of states (TDOS) shown in Figure 4 allowed us to better understand the physical origin of stabilization of alloy elements. Specially, The Fermi energy, number of electrons, and the density of state at Fermi energy of each material are of great

361 importance to capture the physical properties, listed in Table 5. One can discern clearly from
362 Table 5 and Figure 4 that the Fermi energies of W and SAs located at valley of the DOS,
363 corresponding values of DOS are 0.855, 0.545, and 0.590 for W, SA1, and SA2 respectively,
364 implicating that structures of these should be stable. Likewise, the Fermi energies of HEAs
365 located at hillside of the DOS, corresponding value of DOS are 2.055 and 2.604 for HEA1
366 and HEA2 respectively, reveal the destabilization of HEA structures. Overall speaking, the
367 higher DOS at fermi energy will raise the surface energy and the unstable stacking energy
368 for both SA1 and SA2, excluding the surface energies of $\{1\,1\,1\}$ $\{\bar{1}\,1\,0\}$ between SA1 and
369 SA2.

370 *4.2. Effects of irradiation on the behavior of tungsten-based PFMs*

371 The inventory simulation results in Figures 1 and 2 show that the composition of W and
372 W-based alloys will evolve significantly under irradiation, which motivated the exploration
373 of how these changes could impact on properties. Table 2 goes further with the FISPACT-II
374 simulations by including an assessment of the uncertainties associated with the predicted
375 concentrations of each transmutant, which originate from the errors provided alongside the
376 nuclear data library evaluations for individual reaction cross sections. For the TENDL
377 library used in the calculations, uncertainty quantification is performed using Bayesian Monte
378 Carlo (BMC), which combines uncertainties reported in the experimental data with the
379 uncertainties in the nuclear models that are fitted to produce the cross section evaluations,
380 see [95, 96] for details.

381 The uncertainty estimates in Table 2 show that the uncertainties can be significant,
382 particularly for reaction pathways near W, where nuclear data is less well known, or for
383 longer reaction chains where uncertainties are compounded (summed) over several nuclear
384 reactions.

385 The elastic properties of pure W and W-based alloys with irradiation time up to 10 years
386 were plotted in Figure 5. The number of valence electrons per atom of alloys is determined
387 by its composition by using VCA method. From Fig. 9, one can see that the number of
388 valence electrons for the five tungsten-base PFMs will increase with irradiation years.

389 The total electronic density of states (TDOS) shown in Fig. 4 tells us that the Fermi
390 energies of HEAs located at left hillside of the DOS. The effects of irradiation would add
391 valence electrons of materials to move the Fermi energy to higher energy level, close to valley.
392 In this case, materials with lower fermi energy will be more stable in good agreement with
393 all increasing elastic properties of HEAs as well as higher slope of HEA2 than HEA1 (more
394 valence electrons). The consequence of relatively slight change of valence electrons of SAs is
395 the trivial variation of elastic properties compared to HEAs except for C_{44} of SA1.

396 The reduction of lattice constant and the enlargement of bulk modulus are consist
397 with experimental measurements and d-band filling predictions [94] that valence electrons is
398 increasing. And the larger reduction of lattice constant could lead to larger enlargement of
399 the bulk modulus by Fig. 5(a) and Fig. 6(a).

The surface energies and unstable stacking fault energies of W, HEAs and SAs are shown in Fig. 10 as function of irradiation years. And the Rice criterion [93] was used to estimate the ductility of materials by the ratio of γ_s and γ_{us}, shown in Fig. 11. Materials with large ratio will prefer to slip the atomic layer under external stresses. While materials with smaller ratio would rather to crack to generate a new surface [97–99]. Furthermore, in Fig. 10, both γ_s and γ_{us} show an increase as function of irradiation. This behavior can be explained based on the variation of the number of electrons up to 10 years. According to Fig. 9 and Fig. 4, HEA2 obtains more relatively percentage electron than HEA1 and increasing of electron will move the Fermi energy to right in DOS, where, in case of HEAs, Fermi energy moving toward the valley of DOS. Thus, HEAs become more stable with irradiation time, and have higher γ_s and γ_{us}. Similarly, from Fig. 9 and Fig. 4, the electrons increase with irradiation time for SAs and W. Nevertheless, the Fermi energy located at the valley of DOS, and further increasing electrons will make fermi energy move towards hillside of DOS, especially happening to SA2 and W, and negligible for SA1. In this case, materials would become more unstable, and this situation consists with γ_{us} of SA1 barely change with irradiation year comparing with that of W and SA2.

As we mentioned in previous section 3, the changes on the γ_{us} are twice as pronounced as the changes on γ_s, implying that the γ_{us} is the major factor to govern the dislocation-based ductility parameter D of SAs and HEAs for both slip systems. The results of ductility parameter are shown in Fig. 11. This figure shows that HEAs become more brittle with irradiation time, and irradiation will enhance the ductility of W and SA2, for both slip systems respectively. Moreover, SA1 did show the significant variation as the irradiation. From the Fig. 2, we could conclude that increasing ductility of W and SA2 come from the reducing of W elements and the increment of Re in the materials. The more brittle of HEAs is due to the lost of Ta and the generation of W form transmutation. Additionally, the gradient concentration of those during a 10-year irradiation should be contrasted to explain the difference of HEA1 and HEA2. HEA1 has reduction of Cr with 0.19% and generation of V with 0.15%, and HEA2 has reduction of V with 0.12% and generation of Os with 0.18%. Therefore, HEA2 experiences higher decrease of δ_D as it is moving from V to Os with a further distance(it has V, Os, so it starts from Group V to Group VIII)

5. Conclusions

Our first conclusion is that uncertainty propagation is important for nuclear simulations. Even though the irradiation-induced composition changes are not predicted to have a significant impact on material properties in the present work, it will not always be the case – for example, changes in thermal conductivity as a function of transmutation are striking in W [100]. In such cases, it will be vital to include the uncertainties in predictions of material performance – the method exemplified here should be extended to include data-induced uncertainties in neutron transport simulations (neglected here, but already mature, see e.g. [101]) as well as the uncertainties designs of fusion reactors, such as geometry variation

and material (composition) selection.

Our results also suggest that the differences in the properties of the four tungsten-based candidate materials at the beginning of their operation life are more significant than the changes induced by irradiation. This behavior might be induced by the nature of the VCA approach, which assumes a homogeneous distribution of the alloying elements with the definition of the virtual atoms. Such formulation is a limiting factor to properly investigating the role of the microstructure (and not the chemical composition as such) on the mechanical behavior of these materials. A deep understanding of microstructural damage in alloys under neutron irradiation needs further theoretical and experimental investigations. Our current and future efforts are directed toward studying more complete first-principles DFT electronic structure methods to effectively predict the phase stability and the mechanical properties of irradiated PFMs.

Appendix A. Material behavior of the principal alloying elements

Table A1: Compositions of W and W-alloys after the 10-year power-plant first wall irradiation (atomic % concentration units) as predicted by FISPACT-II.

Material elements	W	SA1	SA2	HEA1	HEA2
W	9.666E+01	6.481E+01	6.555E+01	2.748E+01	2.753E+01
Re	1.727	1.159	1.182	4.574E-01	4.614E-01
Ta	9.061E-01	6.076E-01	6.145E-01	2.122E+01	2.119E+01
Os	6.822E-01	4.614E-01	4.665E-01	1.799E-01	1.814E-01
Hf	1.517E-02	1.017E-02	1.029E-02	5.671E-01	5.667E-01
He	1.198E-03	2.863E-02	2.766E-02	4.207E-02	2.857E-02
H	5.718E-03	1.197E-01	1.252E-01	1.550E-01	1.232E-01
Cr	–	2.675E+01	3.084E+01	2.477E+01	6.095E-02
Ti	–	5.877	3.773E-02	2.495E+01	2.498E+01
V	–	1.635E-01	1.885E-01	1.515E-01	2.485E+01
Sc	–	5.025E-03	2.941E-07	2.412E-02	2.144E-02
Ca	–	1.881E-03	7.655E-06	7.995E-03	7.993E-03
Mn	–	1.578E-04	1.818E-04	1.463E-04	2.71E-012
Y	–	–	9.375E-01	–	–
Sr	–	–	1.767E-02	–	–
Zr	–	–	1.103E-03	–	–

Table A2: Theoretical equilibrium lattice parameter, single-crystal elastic constants, and polycrystalline elastic properties for the principal alloying elements of the five tungsten-based PFMs at the beginning of their operational life, i.e., with the chemical compositions shown in Table 1: equilibrium lattice parameters a_0, bulk modulus B, elastic constants C_{ij}, tetragonal shear modulus C', shear modulus (G) and Young's modulus (E).

	a_0 (Å)	C_{11} (GPa)	C_{12} (GPa)	C_{44} (GPa)	B (GPa)	C' (GPa)	G (GPa)	E (GPa)
W	3.1835	512.501	197.906	142.461	302.771	157.298	148.22	382.669
Cr	2.850	491.795	143.543	101.429	259.627	174.126	95.416	255.008
Ta	3.320	262.579	159.921	72.436	194.140	51.329	47.812	132.554
Ti	3.262	87.367	113.411	39.409	104.730	-13.022	-0.300	-0.900
V	3.000	264.370	138.842	23.738	180.685	62.764	26.548	75.925

Table A3: Theoretical surface energy γ_s, unstable stacking fault energy γ_{us}, and dislocation-based ductility parameter D for the five tungsten-based PFMs at the beginning of their operational life, i.e., with the chemical compositions shown in Table 1. The calculations have been performed in both $\{1\,1\,1\}\{\bar{1}\,1\,0\}$ and $\{1\,1\,1\}\{1\,1\,\bar{2}\}$ slip systems.

	system	this work			references		
		γ_s (J/m^2)	γ_{us}(J/m^2)	D	γ_s(J/m^2)	γ_{us}(J/m^2)	D
$\langle 1\,1\,1\rangle\{\bar{1}\,1\,0\}$	W	3.308	1.684	1.961	3.181 [60]	1.633 [60]	
	Cr	3.308	1.530	2.163	3.505 [102]	1.570 [103]	
	Ta	2.502	0.724	3.387	2.685 [104]	0.831 † [105]	
	V	2.788	0.751	3.713	2.428 [106]	0.616 [106]	3.93 [106]
$\langle 1\,1\,1\rangle\{1\,1\,\bar{2}\}$	W	3.762	1.875	2.006	3.367 [60]	1.830 [60]	
	Cr	3.772	1.599	2.359	3.892 [102]	1.634 [103]	
	Ta	3.004	0.871	3.370	2.884 [104]	0.977 † [105]	
	V	3.214	0.895	3.591	2.703 [106]	0.719 [106]	3.76 [106]

† spectral neighbor analysis potential

Table A4: Fermi energy E_F and number of valence electrons for the principal alloying elements of the five tungsten-based PFMs at the beginning of their operational life, i.e., with the chemical compositions shown in Table 1.

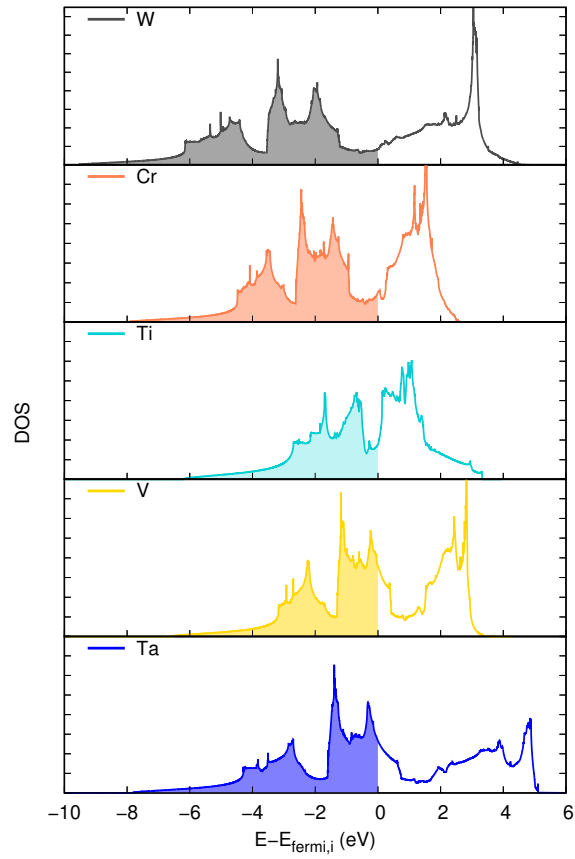|	$E_{F,i}$ (eV)	No. valence e$^-$
W	21.942	14
Cr	19.652	14
Ti	13.370	12
Ta	18.106	13
V	16.628	13

Figure A1: Total DOS of the alloying elements of SAs and HEAs. $E_{F,i}$ is the Fermi energy of each material, and it is taken as the reference energy.

References

[1] Zinkle S J and Ghoniem N M 2011 *Journal of Nuclear Materials* **417** 2–8

[2] Tsai M H and Yeh J W 2014 *Materials Research Letters* **2** 107–123

[3] Li Z, Pradeep K G, Deng Y, Raabe D and Tasan C C 2016 *Nature* **534** 227–230

[4] George E P, Raabe D and Ritchie R O 2019 *Nature reviews materials* **4** 515–534

[5] Murty B S, Yeh J W, Ranganathan S and Bhattacharjee P 2019 *High-entropy alloys* (Elsevier)

[6] Yeh J W, Chen S K, Lin S J, Gan J Y, Chin T S, Shun T T, Tsau C H and Chang S Y 2004 *Advanced engineering materials* **6** 299–303

[7] Leong Z, Wróbel J S, Dudarev S L, Goodall R, Todd I and Nguyen-Manh D 2017 *Scientific Reports* **7** 39803

[8] Waseem O A and Ryu H J 2017 *Scientific reports* **7** 1–14

[9] Zou Y, Ma H and Spolenak R 2015 *Nature communications* **6** 1–8

[10] Senkov O N, Miracle D B, Chaput K J and Couzinie J P 2018 *Journal of materials research* **33** 3092–3128

[11] El-Atwani O, Alvarado A, Unal K, Fensin S, Hinks J, Greaves G, Baldwin J, Maloy S and Martinez E 2021 *Materials Today Energy* **19** 100599

[12] El-Atwani O, Li N, Li M, Devaraj A, Baldwin J, Schneider M M, Sobieraj D, Wróbel J S, Nguyen-Manh D, Maloy S A *et al.* 2019 *Science advances* **5** eaav2002

[13] Senkov O N, Wilks G, Scott J and Miracle D B 2011 *Intermetallics* **19** 698–706

[14] Litnovsky A, Klein F, Tan X, Ertmer J, Coenen J, Linsmeier C, Gonzalez-Julian J, Bram M, Povstugar I, Morgan T, Gasparyan Y M, Suchkov A, Bachurina D, Nguyen-Manh D, Gilbert M G, Sobieraj D, Wróbel J S, Tejado E, Matejicek J, Zoz K, Benz H, Bittner P and Reuban A 2021 *Metals* **11** 1255

[15] Sobieraj D, Wróbel J, Gilbert M R, Litnovsky A, Klein F, Kurzydłowski K J and Nguyen-Manh D 2021 *Metals* **11** 743

[16] Litnovsky A, Wegener T, Klein F, Linsmeier C, Rasinski M, Kreter A, Unterberg B, Vogel M, Kraus S, Breuer U *et al.* 2017 *Nuclear Materials and Energy* **12** 1363–1367

[17] Klein F, Gilbert M R, Litnovsky A, Gonzalez-Julian J, Weckauf S, Wegener T, Schmitz J, Linsmeier C, Bram M and Coenen J W 2020 *Fusion engineering and design* **158** 111667

[18] Koch F and Bolt H 2007 *Physica Scripta* **2007** 100

[19] Sublet J -Ch, Eastwood J W, Morgan J G, Gilbert M R, Fleming M and Arter W 2017 *Nucl. Data Sheets* **139** 77–137

[20] Fleming M, Stainer T and Gilbert M R 2018 The FISPACT-II User Manual Tech. Rep. UKAEA-R(18)001 UKAEA available from http://fispact.ukaea.uk

[21] Tanno T, Hasegawa A, He J, Fujiwara M, Satou M, Nogami S, Abe K and Shishido T 2009 *Journal of Nuclear Materials* **386** 218–221

[22] Tanno T, Fukuda M, Nogami S and Hasegawa A 2011 *Materials transactions* 1105231402–1105231402

[23] Fukuda M, Tanno T, Nogami S and Hasegawa A 2012 *Materials Transactions* **53** 2145–2150

[24] Fukuda M, Hasegawa A, Tanno T, Nogami S and Kurishita H 2013 *Journal of Nuclear Materials* **442** S273–S276

[25] Hasegawa A, Tanno T, Nogami S and Satou M 2011 *Journal of nuclear materials* **417** 491–494

[26] Hasegawa A, Fukuda M, Yabuuchi K and Nogami S 2016 *Journal of Nuclear Materials* **471** 175–183

[27] Fujitsuka M, Tsuchiya B, Mutoh I, Tanabe T and Shikama T 2000 *Journal of nuclear materials* **283** 1148–1151

[28] Garrison L M, Katoh Y, Geringer J W, Akiyoshi M, Chen X, Fukuda M, Hasegawa A, Hinoki T, Hu X, Koyanagi T *et al.* 2019 *Fusion Science and Technology* **75** 499–509

[29] Hwang T, Hasegawa A, Tomura K, Ebisawa N, Toyama T, Nagai Y, Fukuda M, Miyazawa T, Tanaka T and Nogami S 2018 *Journal of Nuclear Materials* **507** 78–86

[30] Katoh Y, Snead L, Garrison L, Hu X, Koyanagi T, Parish C, Edmondson P, Fukuda M, Hwang T, Tanaka T *et al.* 2019 *Journal of Nuclear Materials* **520** 193–207

[31] Edmondson P D, Gault B and Gilbert M R 2020 *Nuclear Fusion* **60** 126013

[32] Nguyen-Manh D, Horsfield A and Dudarev S 2006 *Physical Review B* **73** 020101

[33] Derlet P M, Nguyen-Manh D and Dudarev S 2007 *Physical Review B* **76** 054107

[34] Nguyen-Manh D, Vitek V and Horsfield A 2007 *Progress in materials science* **52** 255–298

[35] Nguyen-Manh D, Lavrentiev M Y, Muzyk M and Dudarev S 2012 *Journal of Materials Science* **47** 7385–7398

[36] Cereceda D, Perlado J M and Marian J 2012 *Computational materials science* **62** 272–275

[37] Dudarev S 2013 *Annual Review of Materials Research* **43** 35–61

[38] Cereceda D 2015 *Univerisdad Politécnica de Madrid (Ph. D. thesis)*

[39] Hofmann F, Nguyen-Manh D, Gilbert M, Beck C, Eliason J, Maznev A, Liu W, Armstrong D, Nelson K and Dudarev S 2015 *Acta Materialia* **89** 352–363

[40] Nguyen-Manh D and Dudarev S 2015 *Nuclear Instruments and Methods in Physics Research Section B: Beam Interactions with Materials and Atoms* **352** 86–91

[41] Cereceda D, Diehl M, Roters F, Raabe D, Perlado J M and Marian J 2016 *International Journal of Plasticity* **78** 242–265

[42] De Vicente S G, Boutard J L, Zinkle S and Tanigawa H 2017 *Nuclear Fusion* **57** 092011

[43] Abernethy R 2017 *Materials Science and Technology* **33** 388–399

[44] Marian J, Becquart C S, Domain C, Dudarev S L, Gilbert M R, Kurtz R J, Mason D R, Nordlund K, Sand A E, Snead L L *et al.* 2017 *Nuclear Fusion* **57** 092008

[45] Mason D R, Nguyen-Manh D and Becquart C S 2017 *Journal of Physics: Condensed Matter* **29** 505501

[46] Dudarev S L, Mason D R, Tarleton E, Ma P W and Sand A E 2018 *Nuclear Fusion* **58** 126002

[47] Mason D R, Nguyen-Manh D, Marinica M C, Alexander R, Sand A E and Dudarev S L 2019 *Journal of Applied Physics* **126** 075112

[48] Nordlund K 2019 *Journal of Nuclear Materials* **520** 273–295

[49] Derlet P M and Dudarev S L 2020 *Phys. Rev. Materials* **4**(2) 023605

[50] Gilbert M R, Arakawa K, Bergstrom Z, Caturla M J, Dudarev S L, Gao F, Goryaeva A, Hu S, Hu X, Kurtz R J *et al.* 2021 *Journal of Nuclear Materials* **554** 153113

[51] Muzyk M, Nguyen-Manh D, Kurzydłowski K J, Baluc N L and Dudarev S L 2011 *Phys. Rev. B* **84**(10) 104115

[52] Muzyk M, Nguyen-Manh D, Wróbel J, Kurzydłowski K, Baluc N and Dudarev S 2013 *Journal of Nuclear Materials* **442** S680–S683

[53] Wei N, Jia T, Zhang X, Liu T, Zeng Z and Yang X 2014 *AIP Advances* **4** 057103

[54] Yang C and Qi L 2018 *Physical Review B* **97** 014107

[55] Huang C H, Gharaee L, Zhao Y, Erhart P and Marian J 2017 *Physical Review B* **96** 094108

[56] Jiang D, Ouyang C and Liu S 2016 *Fusion Engineering and Design* **106** 34–39

[57] Li X, Schönecker S, Li R, Li X, Wang Y, Zhao J, Johansson B and Vitos L 2016 *Journal of Physics: Condensed Matter* **28** 295501

[58] Hu Y J, Shang S L, Wang Y, Darling K A, Butler B G, Kecskes L J and Liu Z K 2016 *Journal of Alloys and Compounds* **671** 267–275

[59] Giusepponi S and Celino M 2013 *Journal of nuclear materials* **435** 52–55

[60] Qian J, Wu C, Fan J and Gong H 2018 *Journal of Alloys and Compounds* **737** 372 – 376 ISSN 0925-8388

[61] Nguyen-Manh D, Wróbel J S, Klimenkov M, Lloyd M J, Messina L and Dudarev S L 2021 *Phys. Rev. Materials* **5**(6) 065401

[62] Suzudo T, Yamaguchi M and Hasegawa A 2014 *Modelling and Simulation in Materials Science and Engineering* **22** 075006

[63] Hossain M and Marian J 2014 *Acta materialia* **80** 107–117

[64] Gharaee L, Marian J and Erhart P 2016 *Journal of Applied Physics* **120** 025901

[65] Giusepponi S and Celino M 2015 *Nuclear Instruments and Methods in Physics Research Section B: Beam Interactions with Materials and Atoms* **342** 70–75

[66] Setyawan W, Nandipati G and Kurtz R J 2017 *Journal of Nuclear Materials* **484** 30–41

[67] Romaner L, Ambrosch-Draxl C and Pippan R 2010 *Physical review letters* **104** 195503

[68] Li H, Wurster S, Motz C, Romaner L, Ambrosch-Draxl C and Pippan R 2012 *Acta materialia* **60** 748–758

[69] Wu X, You Y W, Kong X S, Chen J L, Luo G N, Lu G H, Liu C and Wang Z 2016 *Acta Materialia* **120** 315–326

[70] Fischer U, Bachmann C, Catalan J P, Eade T, Flammini D, Gilbert M, Jaboulay J, Konobeev A, Leichtle D, Lu L, Malouch F, Moro F, Pereslavtsev P, Qiu Y, Sanz J, Sauvan P, Stankunas G, , Travleev A, Turner A, Ogando F, Palermo I and Villari R 2017 *Fus. Eng. Des.* **123** 26–31

[71] Gilbert M R, Eade T, Bachmann C, Fischer U and Taylor N P 2018 *Fus. Eng. Des.* **136** 42–48

[72] Federici G, Kemp R, Ward D, Bachmann C, Franke T, Gonzalez S, Lowry C, Gadomska M, Harman J, Meszaros B, Morlock C, Romanelli F and Wenninger R 2014 *Fus. Eng. Des.* **89** 882 – 889 ISSN 0920-3796 proceedings of the 11th International Symposium on Fusion Nuclear Technology-11 (ISFNT-11) Barcelona, Spain, 15-20 September, 2013

[73] Federici G, Bachmann C, Barucca L, Biel W, Boccaccini L, Brown R, Bustreo C, Ciattaglia S, Cismondi F, Coleman M, Corato V, Day C, Diegele E, Fischer U, Franke T, Gliss C, Ibarra A, Kembleton R, Loving A, Maviglia F, Meszaros B, Pintsuk G, Taylor N, Tran M, Vorpahl C, Wenninger R and You J 2018 *Fus. Eng. Des.* **136** 729 – 741 ISSN 0920-3796 special Issue: Proceedings of the 13th International Symposium on Fusion Nuclear Technology (ISFNT-13)

[74] Qian Y, Gilbert M R, Dezerald L and Cereceda D 2021 *Journal of Physics: Condensed Matter* **33** 345901

[75] Gilbert M and Sublet J C 2011 *Nuclear Fusion* **51** 043005 URL https://doi.org/10.1088/0029-5515/51/4/043005

[76] Gilbert M, Sublet J C and Dudarev S 2017 *Nuclear Fusion* **57** 044002 URL https://doi.org/10.1088/1741-4326/aa5e2e

[77] Sobieraj D, Wróbel J S, Rygier T, Kurzydłowski K J, El Atwani O, Devaraj A, Saez E M and Nguyen-Manh D 2020 *Physical Chemistry Chemical Physics* **22** 23929–23951

[78] Giannozzi P, Baroni S, Bonini N, Calandra M, Car R, Cavazzoni C, Ceresoli D, Chiarotti G L, Cococcioni M, Dabo I *et al.* 2009 *Journal of physics: Condensed matter* **21** 395502

[79] Giannozzi P, Andreussi O, Brumme T, Bunau O, Nardelli M B, Calandra M, Car R, Cavazzoni C, Ceresoli D, Cococcioni M *et al.* 2017 *Journal of Physics: Condensed Matter* **29** 465901

[80] Perdew J P, Burke K and Ernzerhof M 1996 *Physical review letters* **77** 3865

[81] Bellaiche L and Vanderbilt D 2000 *Physical Review B* **61** 7877

[82] Hamann D 2013 *Physical Review B* **88** 085117

[83] Monkhorst H J and Pack J D 1976 *Physical review B* **13** 5188

[84] Koning A J and Rochman D 2017 TENDL-2017 release Date: April 25, 2018. Available from https://tendl.web.psi.ch/tendl_2017/tendl2017.html

[85] Gilbert M R and Sublet J -Ch 2019 *Nuclear Fusion* **59** 086045 URL https://doi.org/10.1088/1741-4326/ab278a

[86] Gilbert M R and Sublet J -Ch 2018 Fusion decay heat validation, FISPACT-II & TENDL-2017, EAF2010, ENDF/B-VIII.0, JEFF-3.3, and IRDFF-1.05 nuclear data libraries Tech. Rep. CCFE-R(18)002 UKAEA available from http://fispact.ukaea.uk

[87] Nguyen-Manh D, Cawkwell M J, Groger R, Mrovec M, Porizek R, Pettifor D G and Vitek V 2005 *Materials Science and Engineering A* **400–401** 68–71

[88] Mrovec M, Gröger R, Bailey A G, Nguyen-Manh D, Elsässer C and Vitek V 2007 *Physical Review B* **75** 104119

[89] Cereceda D, Stukowski A, Gilbert M, Queyreau S, Ventelon L, Marinica M, Perlado J and Marian J 2013 *Journal of Physics: Condensed Matter* **25** 085702

[90] Li Y H, Zhou H B, Liang L, Gao N, Deng H, Gao F, Lu G and Lu G H 2019 *Acta Materialia* **181** 110 – 123 ISSN 1359-6454

[91] Bonny G, Terentyev D, Bakaev A, Grigorev P and Van Neck D 2014 *Modelling and Simulation in*

615   *Materials Science and Engineering* **22** 053001

616 [92] Samolyuk G D, Osetsky Y N and Stoller R E 2012 *Journal of Physics: Condensed Matter* **25** 025403

617 [93] Rice J R 1992 *Journal of the Mechanics and Physics of Solids* **40** 239–271

618 [94] Ayres R, Shannette G and Stein D 1975 *Journal of Applied Physics* **46** 1526–1530

619 [95] Koning A 2015 *Nuclear Data Sheets* **123** 207–213 ISSN 0090-3752 special Issue on International
620   Workshop on Nuclear Data Covariances April 28 - May 1, 2014, Santa Fe, New Mexico,
621   USA http://t2.lanl.gov/cw2014 URL https://www.sciencedirect.com/science/article/pii/
622   S0090375214007157

623 [96] Koning A, Rochman D, Sublet J C, Dzysiuk N, Fleming M and van der Marck S 2019 *Nuclear*
624   *Data Sheets* **155** 1–55 ISSN 0090-3752 special Issue on Nuclear Reaction Data URL https:
625   //www.sciencedirect.com/science/article/pii/S009037521930002X

626 [97] Wang D, Wang C and Yu T 2019 *Royal Society open science* **6** 190441

627 [98] Liu Z G, Wang C Y and Yu T 2013 *Modelling and Simulation in Materials Science and Engineering*
628   **21** 045009

629 [99] Shi S, Zhu L, Zhang H, Sun Z and Ahuja R 2018 *Acta Materialia* **144** 853–861

630 [100] Hofmann F, Mason D M, Eliason J K, Maznev A A, Nelson K A and Dudarev S L 2015 *Sci. Rep.* **5**
631   16042

632 [101] Kos B, Čufar A and Kodeli I A 2021 *Nuclear Engineering and Technology* **53** 2151–2161 ISSN 1738-
633   5733 URL https://www.sciencedirect.com/science/article/pii/S1738573321000553

634 [102] Vitos L, Ruban A, Skriver H L and Kollár J 1998 *Surface science* **411** 186–202

635 [103] Bienvenu B, Fu C C and Clouet E 2020 *Acta Materialia* **200** 570–580

636 [104] Wang J and Wang S Q 2014 *Surface science* **630** 216–224

637 [105] Wang X, Xu S, Jian W R, Li X G, Su Y and Beyerlein I J 2021 *Computational Materials Science* **192**
638   110364

639 [106] Zhang X, Tang J, Deng L, Zhong G, Liu X, Li Y, Deng H and Hu W 2017 *Journal of Alloys and*
640   *Compounds* **701** 975–980